ACS NANO
Cite This: ACS Nano 2018, 12, 12587−12596
www.acsnano.org

ARTICLE

Charge-Transport Mechanisms in $CuInSe_xS_{2-x}$ Quantum-Dot Films

Hyeong Jin Yun,[†] Jaehoon Lim,[†,§,∥] Addis S. Fuhr,[†,‡] Nikolay S. Makarov,[†,∥] Sam Keene,[⊥] Matt Law,[⊥] Jeffrey M. Pietryga,[†] and Victor I. Klimov*[,†]

[†]Chemistry Division, Los Alamos National Laboratory, Los Alamos, New Mexico 87545, United States
[‡]Department of Chemical and Biomolecular Engineering, University of California, Los Angeles, California 90095, United States
[§,∥]Department of Chemical Engineering and Department of Energy System Research, Ajou University, Suwon 16499, Republic of Korea
[∥]UbiQD, Inc., 134 East Gate Drive, Los Alamos, New Mexico 87544, United States
[⊥]Department of Chemistry and Department of Chemical Engineering and Materials Science, University of California, Irvine, California 92697, United States

Supporting Information

ABSTRACT: Colloidal quantum dots (QDs) have attracted considerable attention as promising materials for solution-processable electronic and optoelectronic devices. Copper indium selenium sulfide ($CuInSe_xS_{2-x}$ or CISeS) QDs are particularly attractive as an environmentally benign alternative to the much more extensively studied QDs containing toxic metals such as Cd and Pb. Carrier transport properties of CISeS-QD films, however, are still poorly understood. Here, we aim to elucidate the factors that control charge conductance in CISeS QD solids and, based on this knowledge, develop practical approaches for controlling the polarity of charge transport and carrier mobilities. To this end, we incorporate CISeS QDs into field-effect transistors (FETs) and perform detailed characterization of these devices as a function of the Se/(Se+S) ratio, surface treatment, thermal annealing, and the identity of source and drain electrodes. We observe that as-synthesized $CuInSe_xS_{2-x}$ QDs exhibit degenerate *p*-type transport, likely due to metal vacancies and Cu_{In}'' anti-site defects (Cu^{1+} on an In^{3+} site) that act as acceptor states. Moderate-temperature annealing of the films in the presence of indium source and drain electrodes leads to switching of the transport polarity to nondegenerate *n*-type, which can be attributed to the formation of In-related defects such as $In_{Cu}^{\bullet\bullet}$ (an In^{3+} cation on a Cu^{1+} site) or $In_i^{\bullet\bullet\bullet}$ (interstitial In^{3+}) acting as donors. We observe that the carrier mobilities increase dramatically (by 3 orders of magnitude) with increasing Se/(Se+S) ratio in both *n*- and *p*-type devices. To explain this observation, we propose a two-state conductance model, which invokes a high-mobility intrinsic band-edge state and a low-mobility defect-related intragap state. These states are thermally coupled, and their relative occupancies depend on both QD composition and temperature. Our observations suggest that the increase in the relative fraction of Se moves conduction- and valence band edges closer to low-mobility intragap levels. This results in increased relative occupancy of the intrinsic band-edge states and a corresponding growth of the measured mobility. Further improvement in charge-transport characteristics of the CISeS QD samples as well as their stability is obtained by infilling the QD films with amorphous Al_2O_3 using atomic layer deposition.

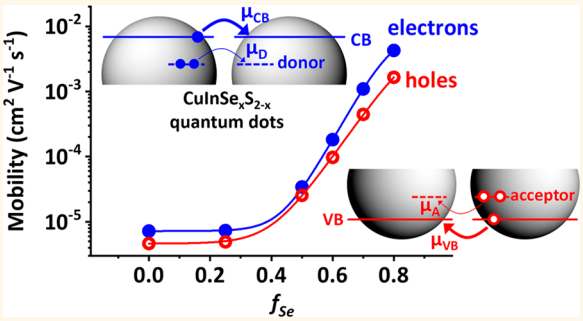

KEYWORDS: *$CuInSe_xS_{2-x}$ quantum dots, field-effect transistor, charge-carrier transport, charge-carrier mobility, n- and p-type, atomic layer deposition*

Colloidal quantum dots (QDs) have been used to demonstrate the viability of various QD-based electronic devices such as field-effect transistors (FETs),[1−3] complementary metal-oxide-semiconductor (CMOS) inverters,[4] logic gates,[5] and wearable electronics.[6] One potentially beneficial distinction of QDs from traditional bulk semiconductors is their amenability toward solution-based processing such as spin coating,[2,6] inkjet printing,[7] and doctor blading,[8] which could enable low-cost, highly flexible (*e.g.*, bendable or foldable) and disposable electronics. The realization of such devices is further simplified by the availability of

Received: September 19, 2018
Accepted: November 29, 2018
Published: November 29, 2018

DOI: 10.1021/acsnano.8b07179
ACS Nano 2018, 12, 12587−12596

demonstrated procedures for tuning both transport polarity and carrier mobility *via* relatively simple and noninvasive post-preparation chemical treatments.[2,4,8−16]

The majority of published charge-transport studies of QD solids have focused on CdE and PbE QDs (most often, E is S or Se). Due to well-developed methodologies for synthesis and assembly of these materials, they are ideally suited for gaining fundamental insights into mechanisms for charge conductance in QD-based mesoscale solids. However, the presence of highly toxic heavy metals (Pb or Cd) limits their practical utility in prospective real-life electronic devices. Copper indium selenium sulfide ($CuInSe_xS_{2-x}$; abbreviated here as CISeS) QDs represent an environmentally benign alternative to Pb- and Cd-based QD materials.[17−22] The available literature studies indicate the feasibility of realizing both *p*- and *n*-type transport polarities in films of CISeS QDs with fairly high mobilities for both electrons and holes (up to ~0.02 $cm^2\ V^{-1}\ s^{-1}$)[19,21] and even ambipolar conductance.[19] These initial observations suggest the considerable potential of these QDs as electronic materials. However, fully exploiting this potential requires a much deeper understanding of their charge-transport properties.

An important distinction of CISeS QDs from PbE and CdE QDs is the presence of two cations and two anions, which makes them prone to a variety of defects that do not occur in binary materials. These defects can affect charge transport by both creating intragap traps and acting as electronic dopants. For instance, metal vacancies (V_{Cu}' and V_{In}''') and a Cu^{1+} cation residing on an In^{3+} site (an antisite Cu_{In}'' defect) represent acceptor states that can enable *p*-type transport.[23,24] However, anion vacancies ($V_S^{\bullet\bullet}$ and $V_{Se}^{\bullet\bullet}$), an In^{3+} cation occupying a Cu^{1+} site (an antisite $In_{Cu}^{\bullet\bullet}$ defect), or an interstitial In cation (an $In_i^{\bullet\bullet\bullet}$ defect) create donor states promoting *n*-type transport.[24] If properly controlled, the abundance of these native defects can allow for manipulating doping levels and transport polarity. This method of defect control can potentially complement or even replace more traditional approaches involving incorporation of impurities[25−27] and various types of surface treatments.[1,3,8,14] It can also allow for the realization of designated transport channels involving engineered defect bands.[28,29]

Here, we investigate carrier transport in films of CISeS QDs with a varied Se/(Se+S) ratio ($f_{Se} = x/2$) incorporated into FETs as a conducting channel. We observe that as-prepared QDs exhibit a *p*-type behavior, while moderate-temperature annealing in the presence of indium imparts *n*-type transport characteristics. Furthermore, we find that increasing f_{Se} leads to improved carrier mobilities in both *n*- and *p*- type QD films and explain this result using a two-state conductance model, in which charge carriers are transported within a QD solid through a high-mobility band formed by intrinsic band-edge states and a low-mobility band created by intragap defects. The f_{Se}-dependent mobility is a result of the f_{Se}-dependent energy spacing between the high- and low-mobility bands, which controls the thermal distribution of carriers between them. In addition, we demonstrate that carrier mobilities, the contrast between the ON and OFF currents, and the air stability of CISeS QD-FETs can be improved by infilling QD films with amorphous Al_2O_3 *via* atomic layer deposition (ALD).

RESULTS AND DISCUSSION

QD Samples and Optical Spectroscopic Studies. We synthesize CISeS QDs with f_{Se} from 0−0.8 following a previously described procedure.[21] According to transmission electron microscopy (TEM) studies (Figures 1a and S1), the QDs have a tetrahedral shape, as previously observed.[17,21,30] Based on X-ray diffraction (XRD) measurements (Figure S2), the prepared QDs exhibit a chalcopyrite crystal structure, with the diffraction peaks shifting toward lower angles with increasing

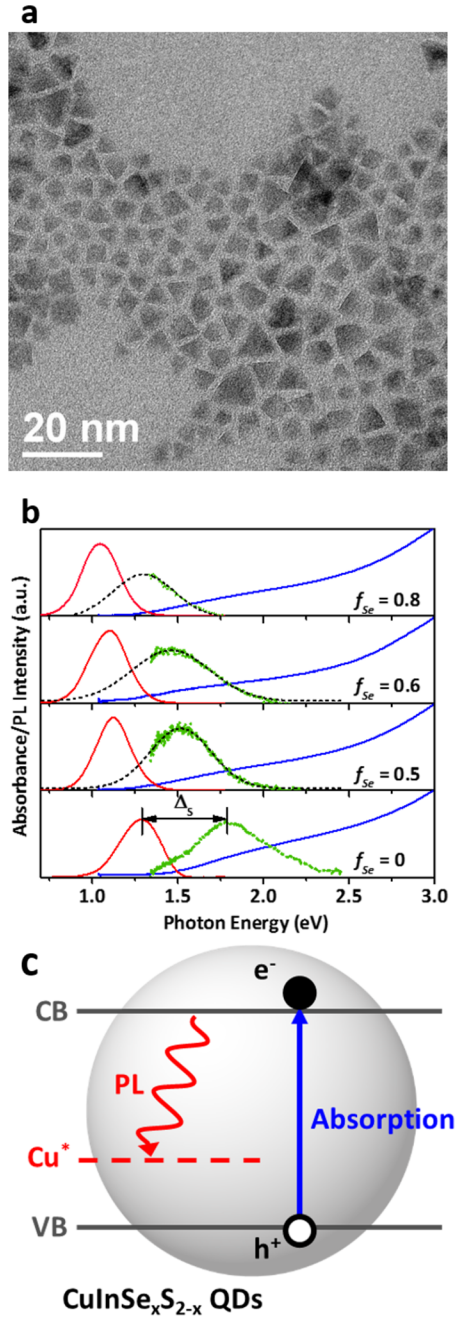

Figure 1. Transmission electron microscopy (TEM) images of $CuInSe_xS_{2-x}$ QDs and their optical spectra. (a) TEM images of $CuInSe_{1.6}S_{0.4}$ QDs with a mean height of 5.5 nm and a standard deviation of 1.8 nm. (b) Optical absorption (blue solid lines), photoluminescence (PL; red solid lines), and early time TA (dotted green lines, 1 ps pump−probe delay; black dashed lines are Gaussian fits) spectra of $CuInSe_xS_{2-x}$ QDs with a varied Se fraction; all samples have approximately the same height of 5.0−5.7 nm. (c) Schematic representation of optical transitions responsible for the VB-to-CB absorption (blue arrow) and intragap PL (red wavy arrow); the latter transition involves a native Cu-related defect (Cu*).

DOI: 10.1021/acsnano.8b07179
ACS Nano 2018, 12, 12587−12596

f_{Se}. This can be explained by the lattice expansion driven by the increased fraction of larger selenium anions. Elemental analysis by inductively coupled plasma optical emission spectroscopy (ICP-OES) indicates that the QDs are anion rich; however, establishing to what degree is complicated by the presence of sulfur in the 1-dodecanethiol (DDT) ligands. The fabricated samples exhibit a Cu/In ratio of 0.95. To focus on the effect of composition without complications due to a varied size, in our studies, we use samples with a similar average QD height (h) of 5.0−5.7 nm (Figure S1).

As is typical for CISeS QDs, absorption spectra of the synthesized samples do not exhibit a sharp band-edge peak but instead show a smooth step (blue lines in Figure 1b). Therefore, to determine the QD band gap (E_g), we apply transient-absorption (TA) spectroscopy and use the position of the lowest-energy (band-edge), early time bleach (dotted green lines in Figure 1b; the pump−probe delay is ∼1 ps) as a measure of E_g.[31] This yields the band gap of 1.80 to 1.34 eV for f_{Se} changing from 0 to 0.8. Consistent with previous observations, the observed photoluminescence (PL) (red lines in Figure 1b) is characterized by a broad spectral profile (∼250 meV full width at half-maximum, fwhm)[32,33] and exhibits a large Stokes shift (Δ_S) of ∼300 to 500 meV *versus* E_g. As f_{Se} increases from 0 to 0.8, the PL peak shifts from 1.3 to 1.0 eV.

In literature, the large PL Stokes shift in CISeS QDs has been explained several ways, including invoking the peculiar electronic structure of chalcopyrite nanocrystals, which features low-oscillator-strength band-edge states,[34] exciton self-localization,[35] and, finally, the involvement of an emissive intragap hole-like state associated with a Cu-related native defect.[23,24,36] According to a recently refined Cu-defect model, altering the QD stoichiometry and thereby the amount of Cu^{2+} *versus* Cu^{1+} defects impacts the dominant emission mechanism.[33] Specifically, in stoichiometric QDs (*i.e.*, Cu/In = 1), where the prevailing defect is an antisite In_{Cu}−Cu_{In} pair, the copper ion is in the Cu^{1+} state with a fully occupied d-shell (d^{10}). To become PL-active, it must first trap a valence-band (VB) hole, and only after that, it can capture a conduction-band (CB) electron *via* a radiative transition. However, Cu-deficient QDs (Cu/In < 1) are characterized by a large abundance of Cu^{2+} defects created as a means of charge compensation for copper vacancies. Because the d^9 Cu^{2+} ion can be considered to have a hole in its *d*-shell prior to excitation, such defects are immediately emission-ready and can participate in radiative recombination without capturing a VB hole. An important element of this model, though, is that the photogenerated hole must be promptly removed from the VB state (due, *e.g.*, to trapping at V_{Cu}'); otherwise, the QD emission would have been dominated not by the intragap Cu-defect-related emission but much faster intrinsic band-to-band radiative recombination.[33] Because the samples we study here are only slightly Cu-deficient, both of these pathways are viable. Accordingly, we simplify our schematic representation of the emission mechanism in Figure 1c by labeling the Cu-related emissive defect as Cu* (where the asterisk can be either 1+ or 2+).

Cyclic Voltammetry Measurements. To quantify absolute energies of electronic states in synthesized QDs, we conduct cyclic voltammetry (CV) measurements (see the Methods section for experimental details). Figure 2a shows an example of CV traces taken for the QD sample with f_{Se} = 0.8, which exhibits the highest *p*-type carrier mobility, as detailed later in this work. Additional CV measurements for samples with varied f_{Se} are shown in Figure S3a. Following the methodology of previous

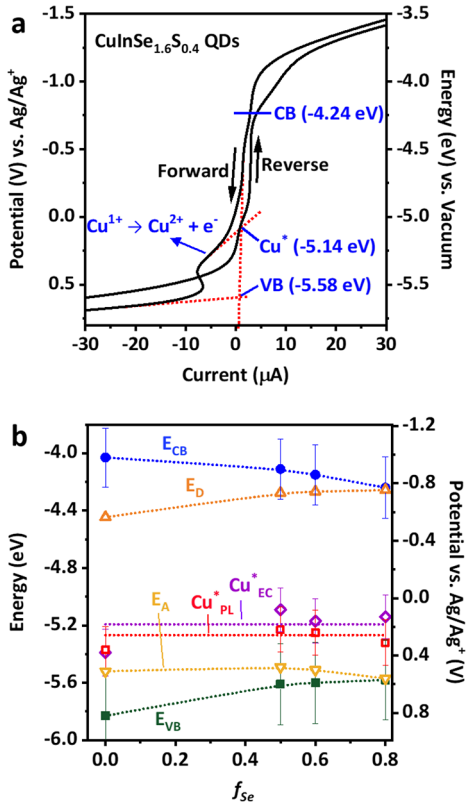

Figure 2. Electrochemical studies of $CuInSe_xS_{2-x}$ QDs and energies of optically and electrically active states as a function of a varied Se content (f_{Se}). (a) Cyclic voltammograms (CVs) of $CuInSe_{1.6}S_{0.4}$ QD colloidal solutions; mean QD height is 5.5 nm. The potential is scanned from 0 to 2 V (forward scan), then to −2 V (reverse scan), and, finally, back to 0 V. An intragap wave with onset at −5.14 V *versus* vacuum (obtained from the intersection of the red dashed lines) observed during the forward scan is ascribed to oxidation of Cu^{1+} to Cu^{2+}. The second oxidation wave with onset at −5.58 V *versus* vacuum is due to hole injection into the QD VB. The position of the CB level is obtained as a sum of the VB energy and the optical band gap. (b) Energies of the CB (blue solid circles) and VB (green solid squares) band-edge levels for $CuInSe_xS_{2-x}$ QDs with different f_{Se} values based on CV and optical measurements. The purple open diamonds (Cu^*_{EC}) show the redox potential of the intragap feature ascribed to the Cu* defect, and the red open squares (Cu^*_{PL}) correspond to the energy of the intragap state obtained based on the apparent Stokes shift (Δ_S) from the optical measurements (Figure 1b). The energies of native donor and acceptor defects obtained from transport measurements are shown by orange open upward-pointing triangles and yellow open downward-pointing triangles, respectively.

CV studies of QDs,[33,37,38] we determine energies of redox-active states from onset potentials of observed CV waves inferred from extrapolations of linear fits (red dotted lines in Figure 2a). For a forward scan, when the electrochemical potential (V_{EC}) is swept to progressively more oxidative values, we detect two distinct oxidation waves. Based on our previous analysis,[33,37] the first wave (+0.13 V *versus* Ag/Ag^+) can be ascribed to the Cu* defect (E_{Cu*}) and the second wave (+0.57 V *versus* Ag/Ag^+) to the VB edge (E_{VB}). In principle, we should be able to determine the CB-edge position (E_{CB}) in a similar manner from the reverse scan. However, as shown in Figure S3b, the parasitic background current from the electrolyte observed at large reductive potentials masks QD-related features. Therefore, we find the CB energy from the sum of the measured VB-edge energy and

DOI: 10.1021/acsnano.8b07179
ACS Nano 2018, 12, 12587−12596

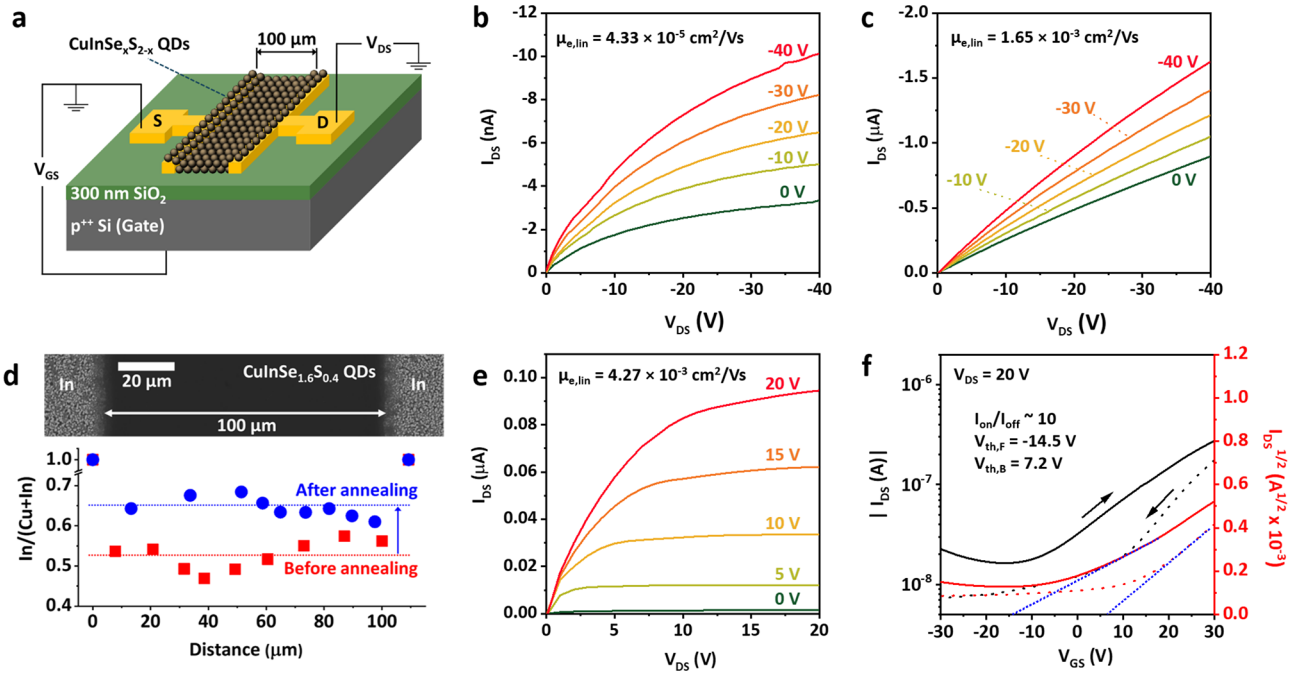

Figure 3. Charge-transport measurements of $CuInSe_{1.6}S_{0.4}$ QD films incorporated into FETs. (a) A schematic representation of a bottom-gate, bottom-contact QD-FET. (b) Output characteristics (I_{DS} *vs* V_{DS}) of a gold-contact FET made of as-synthesized $CuInSe_{1.6}S_{0.4}$ QDs with long native ligands (the mean QD height h = 5.5 nm), which shows a *p*-channel behavior. (c) Output characteristics for a gold-contact FET based on QDs treated with EDT ligands. (d) A top-view SEM image of an In-contact $CuInSe_{1.6}S_{0.4}$ QD-FET along with the plot of the In/(In+Cu) ratio as a function of location along the channel before (red squares) and after (blue circles) heat treatment at 250 °C, as determined by EDS. (e) Output characteristics of the In-contact $CuInSe_{1.6}S_{0.4}$ QD-FET after thermal annealing, which show a non-degenerate *n*-channel behavior. (f) Transfer characteristics (I_{DS} *vs* V_{GS}) of the device shown in "*e*" measured at V_{DS} = 20 V, which corresponds to the saturation regime. Solid and dotted lines are the forward and the reverse scan, respectively. The linear extrapolation of the $(I_{DS})^{0.5}$ transfer curves measured for large positive voltages are used to determine a threshold voltage, V_{th} (blue lines); values $V_{th,F}$ and $V_{th,B}$ are obtained from the forward and reverse (backward) scans, respectively.

the optical band gap inferred from the TA spectra (Figure 1b, dotted green lines).

In Figure 2b, we present a summary of CV and optical measurements of energies of the redox-active intragap state (presumably a Cu* defect) and the VB and CB edges for samples with different Se fractions plotted as a function of f_{Se}. The energies are shown *versus* both vacuum (left vertical axis) and the Ag/Ag^+ potential (right vertical axis). We observe that increasing f_{Se} leads to a drop in E_{CB} (blue solid circles), which is accompanied by an increase in E_{VB} (green solid squares). The energy of the intragap state is determined from both CV measurements (purple open diamonds) and the Stokes shift of the PL band (red open squares).[33] The two data sets are in excellent agreement and indicate that E_{Cu^*} is nearly independent of f_{Se}. Furthermore, the absolute value of E_{Cu^*} (*ca.* −5.22 V *versus* vacuum; average of the PL and CV measurements) is consistent with the $Cu^{1+/2+}$ redox potential,[39−41] confirming the assignment of the intragap state to the Cu-related defect.[33]

Charge-Transport Studies. To investigate charge-transport characteristics of CISeS QD films, we incorporate them into FETs fabricated on heavily doped *p*-type silicon wafers with a thermally grown silicon oxide (300 nm thickness) using a bottom-gate, bottom-source/drain contact configuration (Figure 3a). Source and drain electrodes are applied to the wafer surface *via* thermal evaporation, and colloidal QDs are deposited onto the prepatterned substrate by spin-coating. The typical thickness of the QD layer is ∼100 nm. In some cases (as specified below), long native oleylamine and DDT ligands are replaced with shorter molecules such as 1,2-ethandithiol (EDT) by solution treatment after deposition. Additionally, for some of the measurements, the FET films have undergone thermal annealing according to protocols described later in this work.

Representative output curves (source-drain current, I_{DS}, *versus* source-drain voltage, V_{DS}) of FETs fabricated with gold contacts and QDs with f_{Se} = 0.8 without ligand exchange are presented in Figure 3b. Despite a large average interparticle distance defined by long native ligands (Figure 1a), the QD films show fairly good *p*-type conductance that is well modulated by gate voltage (V_{GS}). Based on the measured $I_{DS}-V_{DS}$ characteristics, we obtain that the hole mobility in the linear regime[2] ($\mu_{h,lin}$) is 4.33×10^{-5} cm^2 V^{-1} s^{-1}. These results are distinct from previously studied FETs based on PbE and CdE QDs, wherein the films of as-deposited QDs are insulating and not gatable prior to ligand exchange. The gatable behavior of the as-deposited CISeS QDs supports our earlier assertion that native defects inherent to these quaternary materials can serve as electron donors or acceptors. Due to this self-doping effect, the Fermi level shifts closer to high-mobility band-edge states, which helps access them by applying gate bias. In this specific case, the observed *p*-channel transport can be ascribed to, for example, metal vacancies and antisite Cu_{In}'' defects

After ligand exchange with EDT, the film mobility increases to $\mu_{h,lin} = 1.65 \times 10^{-3}$ cm^2 V^{-1} s^{-1}; (Figure 3c, gold-contact FET), which is likely a direct result of decreased inter-QD spacing.[11] At the same time, we observe a weakened modulation by V_{GS}, suggesting an increase in hole concentration caused likely by the increase in QD density, which translates into increased dopant concentration (by volume) even if the per-dot number of

DOI: 10.1021/acsnano.8b07179
ACS Nano 2018, 12, 12587−12596

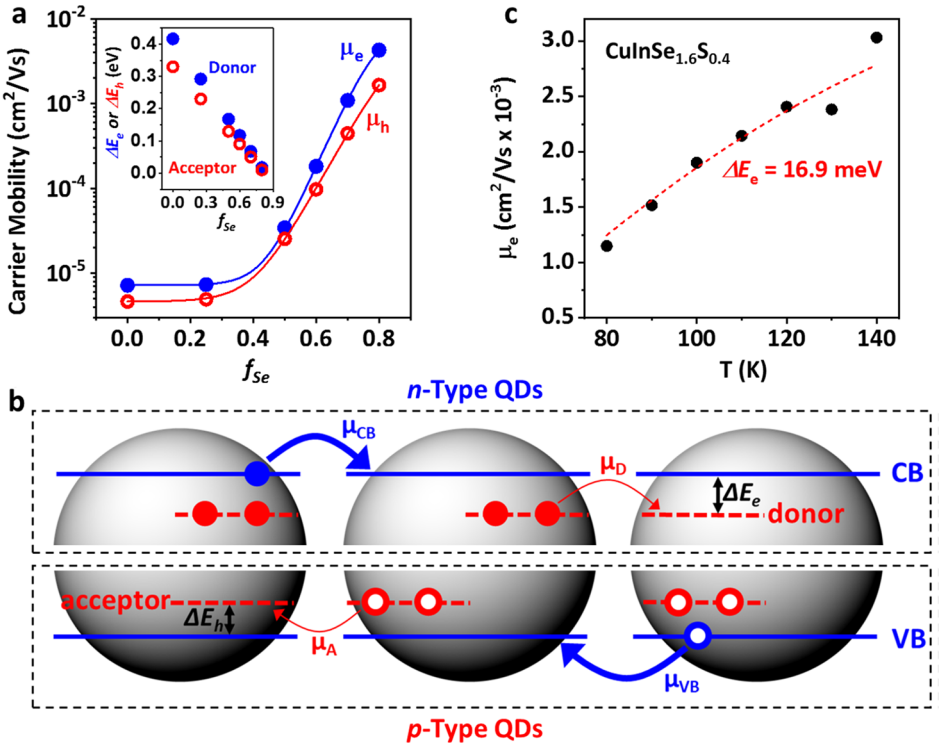

Figure 4. Two-state conductance model. (a) Electron (blue) and hole (red) mobilities obtained from FET measurements of, respectively, *n*- (indium contacts; EDT-treated, annealed QD films) and *p*- (gold contacts; EDT treated QD films) type devices (symbols) in comparison with calculations using a two-state conductance model (lines). The energy gap between the band-edge and the defect states as a function of f_{Se} is displayed in the inset by solid blue (*n*-type films) and open red (*p*-type films) symbols. The absolute energies of defect states derived from charge transport studies are shown in Figure 2b by orange open upward-pointing triangles (donors) and yellow open downward-pointing triangles (acceptors). (b) A schematic depiction of the two-state conductance model for the *n*- (top) and the *p*- (bottom) type $CuInSe_xS_{2-x}$ QD films. In this model, carriers are transported *via* two thermally coupled states. A higher-mobility state is ascribed to the intrinsic CB (*n*-type) or VB (*p*-type) levels (blue) and the lower mobility state to the native donor (*n*-type) or acceptor (*p*-type) defects (red). In thermal equilibrium, the relative occupancies of these states and the resulting apparent mobility are defined by the f_{Se}-dependent interstate energy gap (ΔE_e or ΔE_h) and temperature according to eq 3. (c) Temperature-dependent electron mobility measured in the linear regime for the *n*-type $CuInSe_{1.6}S_{0.4}$ QD film (h = 5.5 nm) (symbols) along with a fit (line) using the two-state conductance mode. The ΔE_e energy produced by this fit (16.9 meV) is virtually identical to that obtained from the room-temperature f_{Se}-dependent measurements (17 meV; the inset of panel a).

dopants remain constant. Specifically, based on the dimensions of our QDs and the lengths of the original (oleylamine and DDT) and final (EDT) ligands, the dot concentration can in principle increase by a factor of >1.5 following surface treatment with EDT. Additionally, the increased hole density can be a result of the doping effect of EDT, which is known to impart *p*-type behavior in PbE QD films.[42,43] Our observations for the CISeS-QD FETs with gold contacts are in agreement with the results of ref 19 for similar devices, which also revealed *p*-type conductance in both as-prepared and EDT-treated films.

It was previously shown that the use of indium source and drain electrodes, followed by thermal annealing after EDT-ligand exchange, leads to devices that exhibit nondegenerate *n*-type transport.[19] Accordingly, we apply indium contacts to a wafer, then spin-coat QDs and after that, treat the QD film with EDT. Afterward, we anneal the complete device at 250 °C for 2 h. Figure 3d shows a top-view scanning electron microscopy (SEM) image of the device channel (QDs with f_{Se} = 0.8) along with a compositional profile obtained using energy-dispersive X-ray spectroscopy (EDS) before (red squares) and after (blue circles) heat treatment. Before annealing, the average In content (as a fraction of the total number of cations, Cu+In) is 52%, which is in agreement with the ICP-OES results for the QDs themselves. However, the In content increases to 65% after annealing, which indicates the diffusion of In throughout the entire device channel. This does not significantly affect the optical absorption of the QD films, and specifically, does not alter the position of the band-edge feature used to quantify the QD band gap (Figure S4). This suggests that the annealing procedures do not lead to sintering of the CISeS particles, which thus preserve their quantum-confined nature.

As seen in the representative output and transfer (I_{DS} *versus* V_{GS}) characteristics (panels e and f of Figure 3, respectively), thermally annealed, In-contact-based QD-FETs show well-modulated *n*-type transport with $\mu_{e,lin} = 4.27 \times 10^{-3}$ cm^2 V^{-1} s^{-1}. The indium-contact annealed devices exhibit a considerable improvement in the ON/OFF current ratio ($I_{on}/I_{off} \approx 10$; Figure 3f) compared with the *p*-type gold-contact based FETs ($I_{on}/I_{off} \approx 3$; Figure S5). We interpret the switch from *p*- to *n*-type conductance as being due to thermal diffusion of In into the QD solid, resulting in the removal of acceptor-type metal-vacancies and/or formation of In-related defects ($In_{Cu}^{\bullet\bullet}$ or $In_i^{\bullet\bullet\bullet}$) acting as donor states.[23,24] For example, as was suggested earlier, a possible source of *p*-doping in as-prepared QDs as well as EDT-treated dots is copper vacancies that trap electrons from the VB leading to generation of VB holes. During annealing in the presence of metallic indium, indium atoms can fill copper vacancies by losing three electrons, one of which reduces the VB hole, while two others are released into the CB. The net result of

DOI: 10.1021/acsnano.8b07179
ACS Nano 2018, 12, 12587−12596

these processes is the transport polarity switching from *p*- to *n*-type.

Charge-Transport Model. Examination of *p*- and *n*-channel devices based on QDs with a varied Se fraction indicates a dramatic effect of f_{Se} on transport characteristics, and in particular, carrier mobilities. Figure S6 shows output characteristics of the *n*-type FETs (indium contacts, annealed) made of QDs with f_{Se} = 0, 0.25, 0.5, 0.6, and 0.7. Electron mobilities derived from these measurements along with the data point for the f_{Se} = 0.8 device (Figure 3e) are plotted in Figure 4a (blue solid circles). These data reveal a dramatic, three-orders-of-magnitude increase in mobility as f_{Se} changes from 0 to 0.8. To explain this observation, we propose a two-state conductance model, wherein carrier transport occurs *via* two distinct states with drastically different mobilities that are separated by an f_{Se}-dependent energy gap (Figure 4b, top). We assume that the higher-energy state is associated with the intrinsic CB-edge level, while the lower energy state is due to a native donor-like defect. This latter state can donate electrons into the CB band *via* thermal excitation. Assuming Maxwell−Boltzmann statistics, we can relate electron occupancies of the CB and donor states (n_{CB} and n_D, respectively) by:

$$n_{CB} = n_D \gamma_{C,D} e^{(-\Delta E_e/k_B T)} \quad (1)$$

where ΔE_e is the energy spacing between the CB and the donor level (the donor ionization energy), $\gamma_{C,D}$ is the ratio of the degeneracy factors of the CB (g_{CB}) and the donor (g_D) states ($\gamma_{C,D} = g_{CB}/g_D$), T is temperature, and k_B is the Boltzmann constant. The intrinsic CB wave function has a considerable extent outside the dot, and as a result, the CB state is characterized by a fairly high mobility (μ_{CB}). However, lower-energy defect-related states are more localized and thus have a poorer mobility ($\mu_D \ll \mu_{CB}$). The effective carrier mobility of this system (μ_e) can be found as a weighted average of the CB- and the defect-state mobilities:

$$\mu_e = \frac{n_{CB}\mu_{CB} + n_D\mu_D}{n_{CB} + n_D} \quad (2)$$

Combining eqs 1 and 2, we obtain the following expression for the T-dependent μ_e:

$$\mu_e = \frac{1}{\gamma_{C,D} e^{(-\Delta E_e/k_B T)} + 1}[\gamma_{C,D}\mu_{CB} e^{(-\Delta E_e/k_B T)} + \mu_D] \quad (3)$$

Next, we use eq 3 to analyze electron mobility data (Figure 4a, blue circles) assuming a linear relationship between ΔE_e and f_{Se}: $\Delta E_e = \Delta E_{e,S} - \beta_e f_{Se}$, where $\Delta E_{e,S}$ is the energy separations between the CB and the donor-like level for purely S-based (*i.e.*, CIS) QDs and β_e is the constant measured in units of energy. We would like to point out that the assumption of the linear dependence of ΔE_e on f_{Se} is approximate and used here because it allows for an accurate description of experimental observations in the studied range of f_{Se}. It is likely not applicable in the case of samples with a high selenium content as for the specific values of $\Delta E_{e,S}$ and β_e obtained below it would produce a negative donor ionization energy for f_{Se} = 1 (CISe QDs).

The saturation of μ_e for f_{Se} below 0.3 suggests that in this range of compositions, ΔE_e is much greater than $k_B T$, and hence, $\mu_e \approx \mu_D = 7.2 \times 10^{-6}$ cm^2 V^{-1} s^{-1} (based on the measured saturated value of μ_e). After quantifying μ_D, we are left with four unknown parameters: μ_{CB}, $\gamma_{C,D}$, $\Delta E_{e,S}$, and β_e. To find them, we solve the system of four equations obtained by substituting μ_e and f_{Se} in eq 3 with experimentally measured values. This yields $\gamma_{C,D} = 1.76$, $\mu_{CB} = 9 \times 10^{-3}$ cm^2 V^{-1} s^{-1}, $\Delta E_{e,S}$ = 416 meV, and β_e = 499 meV. The dependence of μ_e on f_{Se} calculated using these values and eq 3 is shown in Figure 4a (blue solid line), and the f_{Se}-dependent donor-state energies are displayed in Figure 2b (orange open upward-pointing triangles). Given this analysis, a quick increase in μ_e with increasing the fraction of Se in the QDs is due to the reduction in the spacing between the CB and the intragap donor-like state, which leads to the increase in the relative electron occupancy of the high-mobility band-edge state.

To corroborate this model, we have conducted temperature-dependent measurements of the output characteristics of the indium-contact $CuInSe_{1.6}S_{0.4}$ QD-FETs (Figure S7). The mobilities derived from this experiment exhibit a temperature-activated behavior as shown in Figure 4c. By fitting these data to eq 3, we obtain ΔE_e = 16.9 meV. This value is virtually the same as the one obtained from the f_{Se} dependence of the electron mobility (17 meV; inset of Figure 4a).

To study hole transport, we use EDT-treated $CuInSe_xS_{2-x}$ QD-FETs with Au contacts that exhibit *p*-type channel characteristics (Figure S8). The measurements of these devices reveal a strong dependence of hole mobility (μ_h) on f_{Se} (red open circles in Figure 4a), which is similar to that of μ_e (blue solid circles in Figure 4a). In fact, the observed dependence can be quantitatively described by the same model as that presented by eq 3, assuming that the higher-mobility state is associated with a VB hole (mobility μ_{VB}), while the lower mobility state is ascribed to a native acceptor-type defect (mobility μ_A). We denote the energy separation between these states as ΔE_h and the ratio of their degeneracy factors as $\gamma_{V,A}$. Applying the two-state model, we can perfectly describe the hole-transport data in Figure 4 (red line) using the following set of parameters: $\gamma_{V,A}$ = 0.5, $\mu_A = 4.6 \times 10^{-6}$ cm^2 V^{-1} s^{-1}, $\mu_{VB} = 6.4 \times 10^{-3}$ cm^2 V^{-1} s^{-1}, $\Delta E_{h,S}$ = 330 meV, and β_h = 400 meV. As in the previous analysis of electron mobilities, we determine μ_A based on the data for the low-Se-content samples ($f_{Se} < 0.4$), and then find other parameters ($\gamma_{V,A}$, μ_{VB}, $\Delta E_{h,S}$, and β_h) by solving the system of four equations wherein we use four experimental data points for samples with $f_{Se} > 0.4$.

The f_{Se}-dependent acceptor-state energies obtained from this analysis are displayed in Figure 2b by yellow open downward-pointing triangles. As in the case of electron transport, a decrease in the energy spacing between the hole-donating defect and the band-edge state with increasing f_{Se} (compare green squares and open yellow downward-pointing triangles in Figure 2b) leads to a quick (exponential) increase in the apparent hole mobility.

Interestingly, the f_{Se} dependence of the hole mobility closely follows that of the electron mobility. Furthermore, the μ_e and μ_h values for a given Se fraction are also very similar to each other. This close correspondence between electron and hole transport characteristics, while stemming from still unclear reasons (or perhaps being even accidental), is useful from the standpoint of practical applications, as a number electronic devices (*e.g.*, inverters) require electron- and hole-transporting materials with closely matched carrier mobilities.

ALD Infilling. Previously it was shown that ALD infilling of PbSe QD films with amorphous Al_2O_3 could boost carrier mobility and greatly improve air stability of QD samples.[44−46] To test the effect of the ALD treatment on CISeS QD FET performance, we have infilled them with alumina following published procedures.[44] A cross-sectional scanning electron microscope (SEM) image of one such In-contact device

DOI: 10.1021/acsnano.8b07179
ACS Nano 2018, 12, 12587−12596

fabricated from $CuInSe_{1.6}S_{0.4}$ QDs and encapsulated with a *ca.* 20 nm thick layer of Al_2O_3 is displayed in Figure S9. Following alumina infilling, the QD-FET preserves its *n*-type polarity but shows a considerable improvement in both electron mobility (2.5×10^{-2} cm^2 V^{-1} s^{-1} *versus* 4.27×10^{-3} cm^2 V^{-1} s^{-1} before ALD) and the ON/OFF current ratio (~100 *versus* ~ 10 before ALD); compare Figures 3f and 5a,b. Furthermore, we observe an

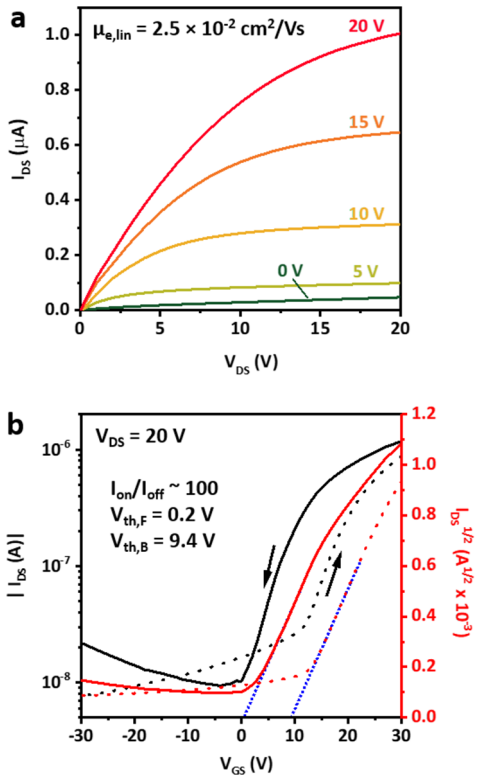

Figure 5. Effect of ALD treatment on characteristics of the *n*-type $CuInSe_{1.6}S_{0.4}$ QD FET. (a) Output characteristics of the ALD-treated indium-contact $CuInSe_{1.6}S_{0.4}$ QD-FET (h = 5.5 nm). (b) Transfer characteristics of the same device. Charge transport parameters are significantly improved upon ALD treatment, as discussed in the text.

inversion in the sign of the threshold voltage (V_{th}) and a considerable reduction in its absolute value (V_{th} = 0.2 V for the ALD-treated device *versus* −14.5 V before the treatment; V_{DS} = 20 V). These results indicate that the ALD procedure enhances the QD film charge transport characteristics in the manner similar to that previously observed for PbSe QD solids.[44,45]

One likely effect of ALD infilling is to passivate surface defect states that lie within the QD band gap, which enhances the carrier mobility by eliminating traps and thereby decreases the average activation energy for carrier transport within the film. In addition, ALD infilling can, in principle, introduce electronic states in the interdot space, which would facilitate dot-to-dot transport if the states' energies are close to the QD band-edge levels. The transport-assisting states can be associated with, for example, intragap defects in alumina and/or an interfacial layer produced by a chemical reaction of Al_2O_3 precursors with the QD surface ligands.

Passivation of QD surface defects due to the ALD procedure also allows for a more complete depletion of a conducting channel under the condition of a lowered Fermi level. This leads to the reduced OFF-current (and hence the improved ON/OFF current ratio) and a considerable reduction of $|V_{th}|$. The ALD-treated devices also exhibit enhanced air stability compared with noninfilled FETs. The ALD-infilled devices maintain their charge-transport characteristics for at least 7 days under ambient conditions (Figure S10), which is a considerable improvement *versus* noninfilled FETs that under similar conditions remain stable only for a few minutes.

The ALD infilling also improves the performance of Au-contact QD-FETs (Figure S11). These devices are originally *p*-type, and interestingly, they maintain their *p*-type characteristics following the ALD procedure. This represents a notable departure from the case of Na_2S-treated PbSe QD films, in which Al_2O_3 infilling changes the polarity of PbSe QD-FETs (from degenerate *p*-type to well-modulated ambipolar), presumably due to passivation of sulfide acceptor states on the QD surfaces.[44] This again suggests that the *p*-type transport polarity of CISeS QD films is not due to surface defects but is instead due to internal acceptor-type states. While not changing transport polarity or the degenerate character of *p*-doping, the ALD treatment boosts hole mobility to 1.55×10^{-2} cm^2/(V s), which is almost a 10-fold improvement compared with non-ALD devices.

CONCLUSIONS

To summarize, we have studied charge-transport characteristics of CISeS QDs incorporated into FETs as a function of a varied anion composition (Se/S ratio), identity of surface ligands, and device type (gold *versus* indium source and drain contacts). Gold-contact FETs made of as-fabricated CISeS QDs with long native ligands exhibit degenerate *p*-type transport due to native acceptor-like defects such as metal vacancies and/or antisite defects (Cu^{1+} on an In^{3+} site). The transport polarity is not altered by either ligand exchange or ALD infilling, supporting the assessment that the *p*-type doping is not due to surface states but rather native defects lattice defects. The transport type can be switched to nondegenerate *n*-type by thermal diffusion of indium throughout the conductive channel realized *via* thermal annealing of indium-contact FETs. This change in transport characteristics likely occurs due to formation of donor-type $In_{Cu}^{\bullet\bullet}$ or $In_i^{\bullet\bullet\bullet}$ defects. The electron and hole mobilities of CISeS QD films show a dramatic, orders-of-magnitude increase with increasing the Se/(Se+S) ratio f_{Se}. To explain this behavior, we propose a two-state transport model wherein charge conductance involves two thermally coupled states with strongly different (by *ca.* a factor of 10^3) mobilities separated by the f_{Se}-dependent energy gap (ΔE_e and ΔE_h). The higher-energy, higher-mobility state is ascribed to the intrinsic QD CB- or VB-edge levels, while the lower-energy, lower-mobility states are associated with native donor (*n*-type films) or acceptor (*p*-type films) defects. The increase in the fraction of Se leads to a reduction of ΔE_e and ΔE_h, which increases the occupancy of higher mobility intrinsic band-edge levels and produces the increase in the apparent carrier mobility. We also demonstrate that transport characteristics and environmental stability of both *p*- and *n*-type films can be enhanced *via* Al_2O_3 ALD infilling without altering the transport polarity. The overall conclusion of these studies is that $CuInSe_xS_{2-x}$ QD films represent a viable, environmentally friendly alternative to films based on Pb- and Cd-containing QDs for applications in solution-processable electronic and optoelectronic devices.

DOI: 10.1021/acsnano.8b07179
ACS Nano 2018, 12, 12587−12596

METHODS AND EXPERIMENTAL

Chemicals and Materials. The following chemicals were purchased and used as received. Anhydrous copper(I) iodide (CuI, 99.995%), 1-dodecanethiol ($CH_3(CH_2)_{11}SH$, DDT, ≥ 98%), selenium (Se, 99.99%), anhydrous octane ($CH_3(CH_2)_6CH_3$, ≥ 99%), anhydrous methanol (CH_3OH, ≥ 99%), anhydrous acetonitrile (CH_3CN, ACN, 99.8%), 1,2-ethanedithiol ($HSCH_2CH_2SH$, EDT, ≥ 98%), tetrabutylammonium perchlorate $(CH_3CH_2CH_2CH_2)_4N(ClO_4)$, $TBAClO_4$, ≥ 99%), and ((3-mercaptopropyl)trimethoxysilane ($HS(CH_2)_3Si(OCH_3)_3$, MPTS, 95%) were obtained from Sigma-Aldrich. Anhydrous indium(III) acetate ($In(CH_3COO)_3$, $In(Ac)_3$, 99.99%) and oleylamine $(CH_3(CH_2)_7CH{=}CH(CH_2)_7CH_2NH_2$, OLAm, 80−90%) were purchased from Acros Organics. 2-Propanol ($(CH_3)_2CHOH$, IPA, 99.5%) and acetone (CH_3COCH_3, 99.5%) were purchased from Fisher Scientific.

Gold (99.99%) and indium (99.99%) evaporation pellets were obtained from Kurt J. Lesker Company. Highly doped p^{+2} Si substrates with thermally grown SiO_2 (300 nm) were purchased from Ossila Ltd.

Synthesis of $CuInSe_xS_{2-x}$ QDs. Typically, 1 mmol of CuI and 1 mmol of $In(Ac)_3$ were dissolved in 5 mL of DDT and 1 mL of OLAm in a 50 mL round-bottom flask, and the mixture was degassed under vacuum at 100 °C for 30 min. Separately, a solution of 1 M Se-OLAm/DDT was prepared by dissolving 1.58 g Se powder in mixture of 15 mL of OLAm and 5 mL of DDT at room temperature in a N_2 glovebox. The temperature of the reactants was raised to 140 °C until all solid precursors were fully dissolved, which usually took less than 10 min. Then, the temperature was raised to 170 °C and 1 M Se-OLAm/DDT (0.5 mL for $CuInSe_{0.5}S_{1.5}$, 1 mL for $CuInSe_{1.0}S_{1.0}$, 1.3 mL for $CuInSe_{1.2}S_{0.8}$, 1.7 mL for $CuInSe_{1.4}S_{0.6}$, and 2 mL for $CuInSe_{1.6}S_{0.4}$ QDs) was added dropwise such that the temperature of the reaction mixture did not vary by more than 3 °C. For nucleation and growth, temperature was set to 230 °C for 60 min. The heating element was then removed, and the QDs were allowed to cool. For synthesizing $CuInS_2$ QDs, the injection of the Se precursor was skipped, and the temperature was raised to 230 °C. The fabricated QDs were purified by iterative dissolution in chloroform and precipitation with methanol and then size-selected by centrifugation at 8000 rpm for 5 min. The resulting QDs were stored in octane under an N_2 atmosphere.

Fabrication of $CuInSe_xS_{2-x}$ QD-FETs. A heavily *p*-doped silicon wafer with a thermally grown silicon oxide (300 nm thickness) was sonicated in DI water (5 min), acetone (5 min), and isopropanol (5 min), then immersed in the MPTS solution (5% in IPA) and held there for 16 h. The MPTS-treated substrates were rinsed with toluene and then sonicated in IPA for 5 min. Metal (Au for *p*-type and In for *n*-type) source and drain bottom contacts (3 mm channel width and 100 μm channel length) were deposited by thermal evaporation (deposition rate of 1 Å s^{-1}) through a shadow mask to achieve a 100 nm thickness. $CuInSe_xS_{2-x}$ QDs dissolved in octane (concentration of ∼20 mg/mL) were spin-coated onto the prepatterned substrate at 1200 rpm. The film was then heated to 150 °C for 10 min in a N_2 glovebox to evaporate the residual solvent. For the EDT treatment, the QD film was immersed in a 1% (by volume) solution of EDT in ACN for 2 min, followed by rinsing with ACN. These QD deposition and ligand-exchange steps were repeated 3 times to yield a total thickness of the QD film of 100 nm. The fabrication of *p*-type FETs was completed by annealing the devices at 100 °C for 30 min in an N_2-filled glovebox to remove any organic residuals. To achieve *n*-type transport polarity, the fabricated indium-contact FETs were annealed at 250 °C for 2 h in an N_2-filled glovebox to facilitate indium diffusion throughout the QD film. For avoiding any deleterious chemical reactions involving oxygen, the O_2 content in the glovebox was thoroughly controlled to ensure it was below 0.1 ppm.

Amorphous Al_2O_3 was deposited in a homemade, cold-wall, traveling-wave ALD system in a glovebox using trimethylaluminum and water as precursors. The substrate temperature was 75 °C and the operating pressure was ∼0.1 Torr. The pulse and the purge times were 40 ms and 90−120 s, respectively. With these parameters, the preparation of a 20 nm ALD film required ∼10 h.

Characterization. TEM images were recorded using a JEOL 2010 TEM equipped with a SC1000 ORIUS CCD camera operating at 120 kV. A top-view SEM and energy-dispersive X-ray spectroscopy (EDS) measurements of $CuInSe_xS_{2-x}$ QD-FETs were performed using a JEOL JSM-IT100 TEM. Cross-sectional SEM studies of ALD-infilled films were conducted on a FEI Magellan 400 XHR SEM. The crystal structure of the QDs was examined by high-resolution X-ray diffraction (Bede D1 System) with the CuKa X-ray source (1.54 Å wavelength) operating at 40 kV and 40 mA. Optical absorption spectra were recorded using a UV−vis−near-infrared (NIR) spectrophotometer (Lambda 950, PerkinElmer). NIR PL spectra were collected using a custom-built apparatus composed of a mechanically chopped 808 nm laser, a grating monochromator, and a liquid N_2-cooled InSb detector coupled to a lock-in amplifier. Elemental analysis was carried out using a Shimadzu ICPE-9000 inductively coupled plasma optical emission spectrometer.

FET characterization was conducted in an N_2-filled glovebox at room temperature using a semiconductor device parameter analyzer (B1500A, Agilent). The probes were placed on top of FET electrodes using a direct current probe positioner.

TA spectra and dynamics were measured in a standard pump−probe configuration using a LabView-controlled home-build setup. The measurements were conducted using 515 nm, 200 fs pump pulses at a 500 Hz repetition rate (second harmonic output of an amplified Yb:KGW laser, Light Conversion Pharos) and a broad-band, white-light supercontinuum probe. The excited-spot diameter was ∼200 μm at the $1/e^2$ level, and the excitation flux was $(1.5{-}9) \times 10^{14}$ photons per square centimeter per second, which corresponded to an average per-dot excitonic occupancy of 0.02−0.1. All measurements were conducted under oxygen-free and moisture-free conditions using airtight quartz cuvettes with vigorous stirring of the sample to minimize photocharging. Samples were prepared in an inert atmosphere in a glovebox.

For electrochemical analyses, an indium tin oxide coated glass slide was used as a working electrode, platinum wire as a counter electrode, and a silver wire as a pseudoreference electrode. $CuInSe_xS_{2-x}$ QDs were diluted to 5 mg/mL in air-free chloroform in a N_2 glovebox. A total of 0.1 M of $TBAClO_4$ was weighed in the glovebox before adding to the QD solution. The QDs:$TBAClO_4$ molar ratio was *ca.* 1:5 so that the electrolyte salt could effectively passivate the QD surface. Cyclic voltammetry (CV) measurements were conducted by loading a QD/electrolyte solution into a quartz cuvette and placing inside it electrodes connected to a computer-controlled potentiostat (CH Instruments). The cuvette was masked with a black tape to eliminate exposure to ambient light. The scan rate was 0.1 V s^{-1}, and data were collected for every 0.001 V for the scan range of 2 to −2 V.

ASSOCIATED CONTENT

Supporting Information

The Supporting Information is available free of charge on the ACS Publications website at DOI: 10.1021/acsnano.8b07179.

Additional TEM images, XRD patterns, CV measurements and optical spectra of $CuInSe_xS_{2-x}$ QDs, additional output and transfer characteristics of gold- and indium-contact FETs, a representative cross-sectional SEM image of a QD-FET, and air-stability studies of non-ALD and ALD-infilled FETs (PDF)

AUTHOR INFORMATION

Corresponding Author

*E-mail: klimov@lanl.gov.

ORCID

Jaehoon Lim: 0000-0003-2623-3550

Jeffrey M. Pietryga: 0000-0001-5360-4228

Victor I. Klimov: 0000-0003-1158-3179

Notes

The authors declare no competing financial interest.

DOI: 10.1021/acsnano.8b07179
ACS Nano 2018, 12, 12587−12596

ACKNOWLEDGMENTS

J.M.P, M.L., S.K., N.S.M., and J.L. were supported by the Center for Advanced Solar Photophysics (CASP), an Energy Frontier Research Center funded by the U.S. Department of Energy (DOE), Office of Science (OS), Basic Energy Sciences (BES). V.I.K. acknowledges support by the Solar Photochemistry Program of the Chemical Sciences, Biosciences and Geosciences Division, BES, OS, DOE. H.J.Y. was supported by the UC Office of the President under the UC Laboratory Fees Research Program Collaborative Research and Training Award LFR-17-477148. A.F. acknowledges support by the African American Partnership Program at Los Alamos National Laboratory.

REFERENCES

(1) Oh, S. J.; Berry, N. E.; Choi, J.-H.; Gaulding, E. A.; Lin, H.; Paik, T.; Diroll, B. T.; Muramoto, S.; Murray, C. B.; Kagan, C. R. Designing High-Performance PbS and PbSe Nanocrystal Electronic Devices through Stepwise, Post-Synthesis, Colloidal Atomic Layer Deposition. *Nano Lett.* **2014**, *14*, 1559−1566.

(2) Hetsch, F.; Zhao, N.; Kershaw, S. V.; Rogach, A. L. Quantum Dot Field Effect Transistors. *Mater. Today* **2013**, *16*, 312−325.

(3) Dolzhnikov, D. S.; Zhang, H.; Jang, J.; Son, J. S.; Panthani, M. G.; Shibata, T.; Chattopadhyay, S.; Talapin, D. V. Composition-Matched Molecular "Solders" for Semiconductors. *Science* **2015**, *347*, 425−428.

(4) Oh, S. J.; Wang, Z.; Berry, N. E.; Choi, J.-H.; Zhao, T.; Gaulding, E. A.; Paik, T.; Lai, Y.; Murray, C. B.; Kagan, C. R. Engineering Charge Injection and Charge Transport for High Performance PbSe Nanocrystal Thin Film Devices and Circuits. *Nano Lett.* **2014**, *14*, 6210−6216.

(5) Stinner, F. S.; Lai, Y.; Straus, D. B.; Diroll, B. T.; Kim, D. K.; Murray, C. B.; Kagan, C. R. Flexible, High-Speed CdSe Nanocrystal Integrated Circuits. *Nano Lett.* **2015**, *15*, 7155−7160.

(6) Choi, J.-H.; Wang, H.; Oh, S. J.; Paik, T.; Sung, P.; Sung, J.; Ye, X.; Zhao, T.; Diroll, B. T.; Murray, C. B.; Kagan, C. R. Exploiting the Colloidal Nanocrystal Library to Construct Electronic Devices. *Science* **2016**, *352*, 205−208.

(7) Haverinen, H. M.; Myllylä, R. A.; Jabbour, G. E. Inkjet Printing of Light Emitting Quantum Dots. *Appl. Phys. Lett.* **2009**, *94*, 073108.

(8) Lin, Q.; Yun, H. J.; Liu, W.; Song, H.-J.; Makarov, N. S.; Isaienko, O.; Nakotte, T.; Chen, G.; Luo, H.; Klimov, V. I.; Pietryga, J. M. Phase-Transfer Ligand Exchange of Lead Chalcogenide Quantum Dots for Direct Deposition of Thick, Highly Conductive Films. *J. Am. Chem. Soc.* **2017**, *139*, 6644−6653.

(9) Talapin, D. V.; Murray, C. B. PbSe Nanocrystal Solids for n- and p-Channel Thin Film Field-Effect Transistors. *Science* **2005**, *310*, 86−89.

(10) Nag, A.; Kovalenko, M. V.; Lee, J. S.; Liu, W.; Spokoyny, B.; Talapin, D. V. Metal-Free Inorganic Ligands for Colloidal Nanocrystals: S^{2-}, HS^{-}, Se^{2-}, HSe^{-}, Te^{2-}, HTe^{-}, TeS_3^{2-}, OH^{-}, and NH^{2-} as Surface Ligands. *J. Am. Chem. Soc.* **2011**, *133*, 10612−10620.

(11) Liu, Y.; Gibbs, M.; Puthussery, J.; Gaik, S.; Ihly, R.; Hillhouse, H. W.; Law, M. Dependence of Carrier Mobility on Nanocrystal Size and Ligand Length in PbSe Nanocrystal Solids. *Nano Lett.* **2010**, *10*, 1960−1969.

(12) Fafarman, A. T.; Koh, W. K.; Diroll, B. T.; Kim, D. K.; Ko, D. K.; Oh, S. J.; Ye, X.; Doan-Nguyen, V.; Crump, M. R.; Reifsnyder, D. C.; Murray, C. B.; Kagan, C. R. Thiocyanate-Capped Nanocrystal Colloids: Vibrational Reporter of Surface Chemistry and Solution-Based Route to Enhanced Coupling in Nanocrystal Solids. *J. Am. Chem. Soc.* **2011**, *133*, 15753−15761.

(13) Boles, M. A.; Ling, D.; Hyeon, T.; Talapin, D. V. The Surface Science of Nanocrystals. *Nat. Mater.* **2016**, *15*, 141−153.

(14) Lee, J.-S.; Kovalenko, M. V.; Huang, J.; Chung, D. S.; Talapin, D. V. Band-Like Transport, High Electron Mobility and High Photoconductivity in All-Inorganic Nanocrystal Arrays. *Nat. Nanotechnol.* **2011**, *6*, 348−352.

(15) Brown, P. R.; Kim, D.; Lunt, R. R.; Zhao, N.; Bawendi, M. G.; Grossman, J. C.; Bulović, V. Energy Level Modification in Lead Sulfide Quantum Dot Thin Films through Ligand Exchange. *ACS Nano* **2014**, *8*, 5863−5872.

(16) Kroupa, D. M.; Vörös, M.; Brawand, N. P.; McNichols, B. W.; Miller, E. M.; Gu, J.; Nozik, A. J.; Sellinger, A.; Galli, G.; Beard, M. C. Tuning Colloidal Quantum Dot Band Edge Positions through Solution-Phase Surface Chemistry Modification. *Nat. Commun.* **2017**, *8*, 15257.

(17) McDaniel, H.; Fuke, N.; Pietryga, J. M.; Klimov, V. I. Engineered $CuInSe_xS_{2-X}$ Quantum Dots for Sensitized Solar Cells. *J. Phys. Chem. Lett.* **2013**, *4*, 355−361.

(18) McDaniel, H.; Fuke, N.; Makarov, N. S.; Pietryga, J. M.; Klimov, V. I. An Integrated Approach to Realizing High-Performance Liquid-Junction Quantum Dot Sensitized Solar Cells. *Nat. Commun.* **2013**, *4*, 1 DOI: 10.1038/ncomms3887.

(19) Draguta, S.; McDaniel, H.; Klimov, V. I. Tuning Carrier Mobilities and Polarity of Charge Transport in Films of $CuInSe_xS_{2-X}$ Quantum Dots. *Adv. Mater.* **2015**, *27*, 1701−1705.

(20) Kim, J.-Y.; Yang, J.; Yu, J. H.; Baek, W.; Lee, C.-H.; Son, H. J.; Hyeon, T.; Ko, M. J. Highly Efficient Copper−Indium−Selenide Quantum Dot Solar Cells: Suppression of Carrier Recombination by Controlled Zns Overlayers. *ACS Nano* **2015**, *9*, 11286−11295.

(21) McDaniel, H.; Koposov, A. Y.; Draguta, S.; Makarov, N. S.; Pietryga, J. M.; Klimov, V. I. Simple yet Versatile Synthesis of $CuInSe_xS_{2-X}$ Quantum Dots for Sunlight Harvesting. *J. Phys. Chem. C* **2014**, *118*, 16987−16994.

(22) Lim, Y. S.; Kwon, H.-S.; Jeong, J.; Kim, J. Y.; Kim, H.; Ko, M. J.; Jeong, U.; Lee, D.-K. Colloidal Solution-Processed $CuInSe_2$ Solar Cells with Significantly Improved Efficiency up to 9% by Morphological Improvement. *ACS Appl. Mater. Interfaces* **2014**, *6*, 259−267.

(23) Ueng, H. Y.; Hwang, H. L. The Defect Structure of $CuInS_2$. Part I: Intrinsic Defects. *J. Phys. Chem. Solids* **1989**, *50*, 1297−1305.

(24) Dagan, G.; Abou-Elfotouh, F.; Dunlavy, D. J.; Matson, R. J.; Cahen, D. Defect Level Identification in Copper Indium Selenide ($CuInSe_2$) from Photoluminescence Studies. *Chem. Mater.* **1990**, *2*, 286−293.

(25) Choi, J.-H.; Fafarman, A. T.; Oh, S. J.; Ko, D.-K.; Kim, D. K.; Diroll, B. T.; Muramoto, S.; Gillen, J. G.; Murray, C. B.; Kagan, C. R. Bandlike Transport in Strongly Coupled and Doped Quantum Dot Solids: A Route to High-Performance Thin-Film Electronics. *Nano Lett.* **2012**, *12*, 2631−2638.

(26) Talapin, D. V.; Lee, J.-S.; Kovalenko, M. V.; Shevchenko, E. V. Prospects of Colloidal Nanocrystals for Electronic and Optoelectronic Applications. *Chem. Rev.* **2010**, *110*, 389−458.

(27) Gresback, R.; Kramer, N. J.; Ding, Y.; Chen, T.; Kortshagen, U. R.; Nozaki, T. Controlled Doping of Silicon Nanocrystals Investigated by Solution-Processed Field Effect Transistors. *ACS Nano* **2014**, *8*, 5650−5656.

(28) Mycielski, J. Mechanism of Impurity Conduction in Semiconductors. *Phys. Rev.* **1961**, *123*, 99−103.

(29) Brawand, N. P.; Goldey, M. B.; Vörös, M.; Galli, G. Defect States and Charge Transport in Quantum Dot Solids. *Chem. Mater.* **2017**, *29*, 1255−1262.

(30) Zang, H.; Li, H.; Makarov, N. S.; Velizhanin, K. A.; Wu, K.; Park, Y.-S.; Klimov, V. I. Thick-Shell $CuInS_2$/ZnS Quantum Dots with Suppressed "Blinking" and Narrow Single-Particle Emission Line Widths. *Nano Lett.* **2017**, *17*, 1787−1795.

(31) Li, L.; Pandey, A.; Werder, D. J.; Khanal, B. P.; Pietryga, J. M.; Klimov, V. I. Efficient Synthesis of Highly Luminescent Copper Indium Sulfide-Based Core/Shell Nanocrystals with Surprisingly Long-Lived Emission. *J. Am. Chem. Soc.* **2011**, *133*, 1176−1179.

(32) Meinardi, F.; McDaniel, H.; Carulli, F.; Colombo, A.; Velizhanin, K. A.; Makarov, N. S.; Simonutti, R.; Klimov, V. I.; Brovelli, S. Highly Efficient Large-Area Colourless Luminescent Solar Concentrators Using Heavy-Metal-Free Colloidal Quantum Dots. *Nat. Nanotechnol.* **2015**, *10*, 878−885.

(33) Fuhr, A. S.; Yun, H. J.; Makarov, N. S.; Li, H.; McDaniel, H.; Klimov, V. I. Light Emission Mechanisms in $CuInS_2$ Quantum Dots Evaluated by Spectral Electrochemistry. *ACS Photonics* **2017**, *4*, 2425−2435.

DOI: 10.1021/acsnano.8b07179
ACS Nano 2018, 12, 12587−12596

(34) Shabaev, A.; Mehl, M. J.; Efros, A. L. Energy Band Structure of $CuInS_2$ and Optical Spectra of $CuInS_2$ Nanocrystals. *Phys. Rev. B: Condens. Matter Mater. Phys.* **2015**, *92*, 035431.
(35) Knowles, K. E.; Nelson, H. D.; Kilburn, T. B.; Gamelin, D. R. Singlet−Triplet Splittings in the Luminescent Excited States of Colloidal Cu+:CdSe, Cu+:InP, and $CuInS_2$ Nanocrystals: Charge-Transfer Configurations and Self-Trapped Excitons. *J. Am. Chem. Soc.* **2015**, *137*, 13138−13147.
(36) Krustok, J.; Schön, J. H.; Collan, H.; Yakushev, M.; Mädasson, J.; Bucher, E. Origin of the Deep Center Photoluminescence in $CuGaSe_2$ and $CuInS_2$ Crystals. *J. Appl. Phys.* **1999**, *86*, 364−369.
(37) Zhong, H.; Lo, S. S.; Mirkovic, T.; Li, Y.; Ding, Y.; Li, Y.; Scholes, G. D. Noninjection Gram-Scale Synthesis of Monodisperse Pyramidal $CuInS_2$ Nanocrystals and Their Size-Dependent Properties. *ACS Nano* **2010**, *4*, 5253−5262.
(38) Akkerman, Q. A.; Genovese, A.; George, C.; Prato, M.; Moreels, I.; Casu, A.; Marras, S.; Curcio, A.; Scarpellini, A.; Pellegrino, T.; Manna, L.; Lesnyak, V. From Binary Cu_2S to Ternary Cu−In−S and Quaternary Cu−In−Zn−S Nanocrystals with Tunable Composition *via* Partial Cation Exchange. *ACS Nano* **2015**, *9*, 521−531.
(39) Sanz, L.; Palma, J.; García-Quismondo, E.; Anderson, M. The Effect of Chloride Ion Complexation on Reversibility and Redox Potential of the Cu(II)/Cu(I) Couple for Use in Redox Flow Batteries. *J. Power Sources* **2013**, *224*, 278−284.
(40) Bard, A. J.; Faulkner, L. R. *Electrochemical Methods*; Wiley: New York, 2001.
(41) Hoffeditz, W. L.; Katz, M. J.; Deria, P.; Cutsail, G. E., III; Pellin, M. J.; Farha, O. K.; Hupp, J. T. One Electron Changes Everything. A Multispecies Copper Redox Shuttle for Dye-Sensitized Solar Cells. *J. Phys. Chem. C* **2016**, *120*, 3731−3740.
(42) Nagpal, P.; Klimov, V. I. Role of Mid-Gap States in Charge Transport and Photoconductivity in Semiconductor Nanocrystal Films. *Nat. Commun.* **2011**, *2*, 486.
(43) Klem, E. J. D.; Shukla, H.; Hinds, S.; MacNeil, D. D.; Levina, L.; Sargent, E. H. Impact of Dithiol Treatment and Air Annealing on the Conductivity, Mobility, and Hole Density in PbS Colloidal Quantum Dot Solids. *Appl. Phys. Lett.* **2008**, *92*, 212105.
(44) Liu, Y.; Tolentino, J.; Gibbs, M.; Ihly, R.; Perkins, C. L.; Liu, Y.; Crawford, N.; Hemminger, J. C.; Law, M. PbSe Quantum Dot Field-Effect Transistors with Air-Stable Electron Mobilities above 7 $cm^2 V^{-1}s^{-1}$. *Nano Lett.* **2013**, *13*, 1578−1587.
(45) Liu, Y.; Gibbs, M.; Perkins, C. L.; Tolentino, J.; Zarghami, M. H.; Bustamante, J.; Law, M. Robust, Functional Nanocrystal Solids by Infilling with Atomic Layer Deposition. *Nano Lett.* **2011**, *11*, 5349−5355.
(46) Zhao, Q.; Zhao, T.; Guo, J.; Chen, W.; Zhang, M.; Kagan, C. R. The Effect of Dielectric Environment on Doping Efficiency in Colloidal PbSe Nanostructures. *ACS Nano* **2018**, *12*, 1313−1320.

DOI: 10.1021/acsnano.8b07179
ACS Nano 2018, 12, 12587−12596